JMEPEG (2010) 19:194–206
DOI: 10.1007/s11665-009-9476-9

Distortion Analysis of Axial Contraction of Carburized-Quenched Helical Gear

Arif Sugianto, Michiharu Narazaki, Minoru Kogawara, Soo Young Kim, and Satoshi Kubota

(Submitted April 17, 2008; in revised form April 8, 2009)

An automotive component (steering helical gear) made from low-alloy structural steel SCr420H was gas-carburized and oil-quenched. Axial contraction of total length was measured after such case-hardening process. Using DEFORM-HT Ver 6.1 simulation tool incorporating phase transformation kinetics, the causal factor of negative axial distortion is studied. Analysis of time-dependent displacement, temperature, phase transformation, and stress-strain generation is presented. Total strain and individual strain (e.g., thermal, elastic, plastic, phase transformation, and transformation plasticity strain) are included. Three simulations consisting of case hardening with transformation plasticity (TP), case hardening without TP, and through hardening with TP were conducted to asses the influence of transformation plasticity and martensite as well as retained austenite in contributing the axial contraction of total length. Finally, transformation plasticity has a greater influence than volume fraction of martensite and retained austenite in producing the negative axial distortion.

Keywords case hardening, computer simulation, distortion, helical gear, through hardening, transformation plasticity

1. Introduction

Gas carburizing followed by oil quenching in general play as a key-role in manufacturing process of a commercial steel part, such as cold-forged precision helical gear for automotive steering components. Minimizing distortion and enhancing compressive residual stress are the important issues for fabricating a high quality gear. The capability of computer simulation tool in monitoring time-dependent property prediction and in analyzing the causal factor of residual stress and strain generation has been shown previously for predicting radial displacement of a helical gear (Ref 1). Due to limitation of presentation space in previous work, the purpose of this report is to predict the distribution of microstructure, distortion, and residual stress in axial direction. The interesting factor to be presented in this study is that the gear has substantial negative axial displacement that causes contraction axially. It is because with same geometry, forging process, and through oil quenching process but different material (steel S45C), the gear underwent expansion or positive displacement in axial direction (Ref 2). To assist the understanding of the effect of carburizing and diffusing carbon into case depth of the carburized layer, a virtual through oil quenching was conducted. This was done due to the fact that thickness of the hardened layer (case depth) had a significant impact on the magnitude of distortion of a heat-treated helical gear (Ref 3).

DEFORM-HT Ver 6.1 simulation tool has a capability of analyzing the stress-strain generation during carburizing-quenching process (Ref 4). Gas carburizing oil quenching process has benefit in increasing compressive residual stress and decreasing unwanted distortion. This tool will be used for investigating the causal factor of axial contraction by analyzing time-dependency of temperature, microstructure, stress, total strain, and individual strain, e.g., thermal strain, elastic strain, plastic strain, phase transformation strain, and transformation plasticity strain. Three-dimensional analysis of stress-strain change on complex shape of this helical gear having shank and gear profile will be much more challenging (Ref 5). In addition, the most common carburized-quenched steel parts from simple shape to complex shape will be in axial expansion. Axial expansion has been observed after carburizing and quenching of simple shape such as cylinder (Ref 6), ring (Ref 7), and ring gear blank (Ref 8). Both Ju et al. and Mukai and Ju reported that an individual tooth of gear shaft and helical gear was in axial expansion after carburizing and quenching, respectively (Ref 9, 10). Cho et al. analyzed the axial expansion of an automotive bevel gear after heat treatment of both forged gear and machined gear. Forged gear had more distorted than machined gear because distortion due to a relaxation of the residual stress by cold forging was not negligible (Ref 11). Both Sugimoto et al. and Rakhit presented a bending tendency after heat treating hypoid gear and pinion gear, respectively, from which it could indicate that the axial displacement was in expansion (Ref 12, 13). In order to analyze the causal factor of negative axial displacement on this studied helical gear, the role of transformation plasticity and magnitude of martensite and retained austenite in suppressing the distortion axially will be investigated by conducting three simulations.

Arif Sugianto, Graduate School of Engineering, Utsunomiya University, Yoto 7-1-2, Utsunomiya, Tochigi 321-8585, Japan; **Michiharu Narazaki** and **Minoru Kogawara**, Department of Mechanical Systems Engineering, Utsunomiya University, Yoto 7-1-2, Utsunomiya, Tochigi 321-8585, Japan; and **Soo Young Kim** and **Satoshi Kubota**, Solution Engineering Group, Yamanaka Engineering Co. Ltd., Ohsaku 2-11-2, Sakura, Chiba 285-0802, Japan. Contact e-mail: narazaki@cc.utsunomiya-u.ac.jp.

2. Experimental Procedure

Figure 1 shows the helical gear in complete configuration (LH side) and in detail dimension consisting of shank and gear facing downward (RH Side). This downward setting is the same as the actual racking system used during stress-relief annealing, carburizing, and quenching processes. The weight percentage of the analytical value of the chemical composition is 0.21C, 0.26Si, 0.82Mn, 0.016P, 0.017S, 0.020Ni, 1.15Cr, 0.01Mo, and Fe as the remainder. Detail of the analytical value compared to the JIS standard is given in Table 1. The important specifications of the gear are, e.g., number of teeth: 6, module: 1.9 mm, helix angle: −22°, and pressure angle: 20°.

In addition to preparing the SCr420H helical gear, there were two specimens prepared for this study, e.g., SUS304 gear blank (Fig. 2) and 10 mm diameter 30 mm long silver probe (JIS K2242 B type). For measuring thermal history, sheathed CA thermocouple was inserted in the center of a silver probe, whereas nine thermocouples (1.0 mm diameter) were wedged into 1.1 mm drilled hole of a SUS304 gear blank as shown in Fig. 2.

3. Simulation Procedure

The entire simulation procedure can be classified into following four major parameters, namely, heat conduction and diffusion, phase transformation kinetics, model and boundary conditions, and stress-strain relationships. The results given by these parameters are the distribution of thermal history (cooling curve and cooling rate curve), microstructure, hardness, and carbon content in which excellent agreement was obtained between predicted and measured results (Ref 14). To analyze the effect of transformation plasticity and martensite as well as retained austenite due to carbon deposit layer-induced hardenability in the case depth on the prediction accuracy, there are three simulations conducted in this study, e.g., case hardening incorporating transformation plasticity (simulation #1), case hardening not incorporating transformation plasticity (simulation #2), and through hardening incorporating transformation plasticity (simulation #3). Heating condition is the same between simulations #1 and #2, and cooling condition including the boundary conditions is same among three simulations.

3.1 Heat Conduction and Diffusion

During the cycle process of heat treating, calculation of metallic-thermal-mechanical coupling was conducted considering the effect of carbon content and incorporating multiphase transformation models. Denoting the volume fraction of the Ith constituent as ξ_I, the mechanical and physical properties χ are assumed to be expressed by the mixture law as a linear combination of the properties χ_I of the constituents of the steel (Ref 15).

$$\chi = \sum_{I=1}^{N} \chi_I(T, C)\xi_I \quad \text{and} \quad \sum_{I=1}^{N} \xi_I = 1 \qquad \text{(Eq 1)}$$

Here, ξ_I and $\chi_I(T, C)$ denote the volume fraction and the material parameter depending on temperature and carbon content of the I-th phase consisting of austenite, bainite, and martensite ξ_A, ξ_B, ξ_M, respectively.

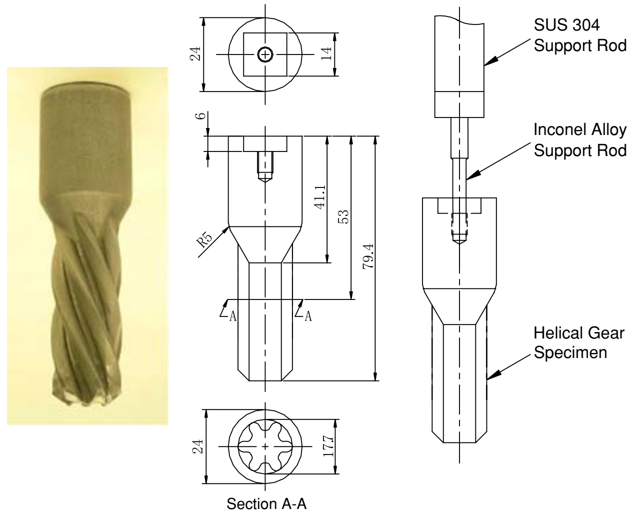

Fig. 1 Configuration and detail dimension of SCr420H helical gear during stress-relief annealing, carburizing, and oil quenching

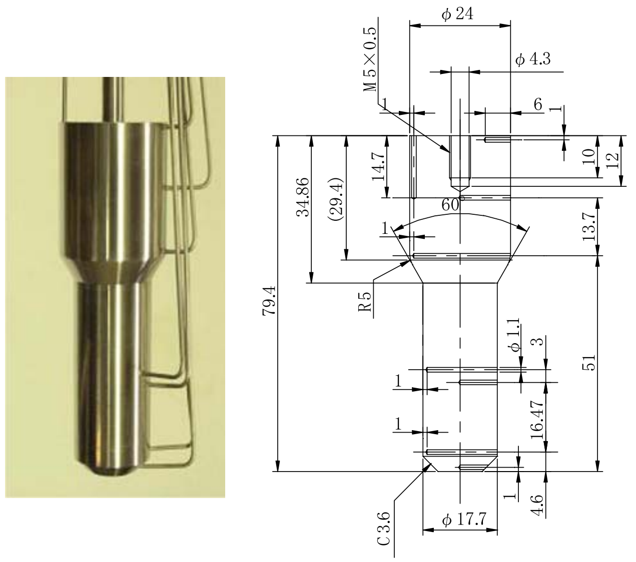

Fig. 2 Configuration and detail dimension of SUS304 gear blank

Table 1 Chemical composition of low alloy steel SCr420H

Element content	C	Si	Mn	P	S	Ni	Cr	Mo	Fe
Analytical value, %	0.21	0.26	0.82	0.016	0.017	0.02	1.15	0.010	Balance
JIS SCr420H, %	0.18-0.23	0.15-0.35	0.60-0.85	<0.030	<0.030	···	0.90-1.20	···	Balance

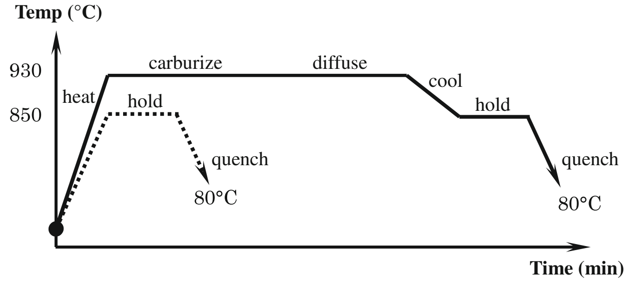

Fig. 3 Simulated heat treatment process for case hardening by gas carburizing oil quenching (*continues line*) and through hardening by oil quenching (*dotted line*)

The temperature field is governed by a special heat conduction equation coupled with the heat generation due to working stress and latent heat due to phase transformation (Ref 16).

$$\rho c\dot{T} - \frac{\partial}{\partial x_i}\left(k\frac{\partial T}{\partial x_i}\right) - \sigma_{ij}\dot{\varepsilon}^{p}_{ij} + \sum \rho_I l_I \dot{\xi}_I = 0 \qquad \text{(Eq 2)}$$

Here, ρ, c, k, and l_I denote the density, the specific heat, the conductivity constant, and the latent heat produced by the progressive I-th constituent. The boundary condition of heat transfer on the outer surface is assumed to be:

$$-k\frac{\partial T}{\partial x_i}n_i = h(T_s - T_\infty) \qquad \text{(Eq 3)}$$

Here, h is a function depends on surface temperature. h, T_s, and T_∞ denote the coefficient of heat transfer, the surface temperature, and the coolant temperature on heat transfer boundary with unit normal n_i, respectively.

During heating to elevated temperature 930 °C for gas carburizing oil quenching process and 850 °C for through oil quenching process (Fig. 3), the specimen is initially assumed to be 100% bainite and the heat up mode is uniform heating. By achieving lower and upper critical temperature, bainite will transform to austenite that is assumed to be simplified diffusion as follows:

$$\xi_A = 1 - \exp\left\{A\left[\frac{T - A_{C1}}{A_{C3} - A_{C1}}\right]^D\right\} \qquad \text{(Eq 4)}$$

Here, ξ_A is the austenite volume fraction, coefficients A and D are taken from dilatation diagram, T is the average element temperature, A_{C1} and A_{C3} are the lower and upper critical temperature taken from IT/TTT diagram, respectively.

As shown in Fig. 3, during carburization and diffusion process only, the gear is case hardened by heating it to above the Ae3 temperature and let the carbon-rich environment increase the carbon concentration on the case. At elevated temperature, the diffusivity of carbon in the case is high and a carbon gradient develops easily, therefore it will produce high carbon content in the case. Depending on the affinity of carbon to the microstructure phase, when carbon is introduced into the steel, the lattice parameters will change (Ref 17). Assuming nonsteady-state practical carburizing, the basic governing equation of the carbon diffusion into the iron matrix is known as Fick's second law (Ref 18).

Table 2 Employed carbon content from external environment as function of carburizing time

Time, s	Environment carbon, %	Time, s	Environment carbon, %
1800	1.1	9001	0.85
9000	1.1	19800	0.85

$$\frac{\partial C}{\partial t} = \frac{\partial}{\partial x_i}\left[D\frac{\partial C}{\partial x_i}\right] \qquad \text{(Eq 5)}$$

Here, D, C, t, and x_i are the diffusion coefficient, the carbon content, the carburizing time, and the position direction. When the diffusion coefficient is assumed to be constant and independent of the composition, Eq 5 can be simplified to:

$$\frac{\partial C}{\partial t} = D\frac{\partial^2 C}{\partial x_i^2} \qquad \text{(Eq 6)}$$

Generally, the diffusion coefficient, D is determined by the boundary condition being specified by the reaction across the surface layer and it is expressed in:

$$D\frac{\partial C}{\partial x_i}n_i = h_c(C_e - C_s) \qquad \text{(Eq 7)}$$

Here, h_c is the coefficient of surface reaction rate which is assumed constant 0.00025 mm/s, C_e is the employed carbon content from external environment during gas carburizing, and C_s is the carbon content in the surface. D is known to be temperature dependent according to expression (8).

$$D \equiv f(C_e, t) \qquad \text{(Eq 8)}$$

Here, C_e is the employed carbon content and t is the carburizing time. The value of each is shown in Table 2.

3.2 Phase Transformation Kinetics

During quenching from 850 °C, there are two reactions, e.g., martensitic reaction and bainitic reaction. Phase change from austenite to martensite is assumed as diffusionless transformation depending on temperature, stress, and carbon content according to Ms 0% and Ms 50% of transformed martensite indicating that, starting from Ms temperature, austenite has been transformed into 0% and 50% volume fraction of martensite, respectively (Fig. 4) and the modified Magee's rule for martensitic reaction (Ref 19).

$$\xi_M = 1 - \exp\left(\psi_1 T + \psi_2(C - C_0) + \psi_{31}\sigma_{ij} + \psi_{32}J_2^{1/2} + \psi_4\right) \qquad \text{(Eq 9)}$$

Here, ξ_M is the volume fraction of martensite that is the function of carbon content, temperature, and stress. J_2 is the second invariant of shear stress. $\psi_1, \psi_2, \psi_3, \psi_4$ are all coefficients obtained from experiments.

Phase change from austenite into bainite is assumed as diffusion or isothermal transformation (TTT curves) according to the following Johnson-Mehl equation for bainitic reaction (Ref 20).

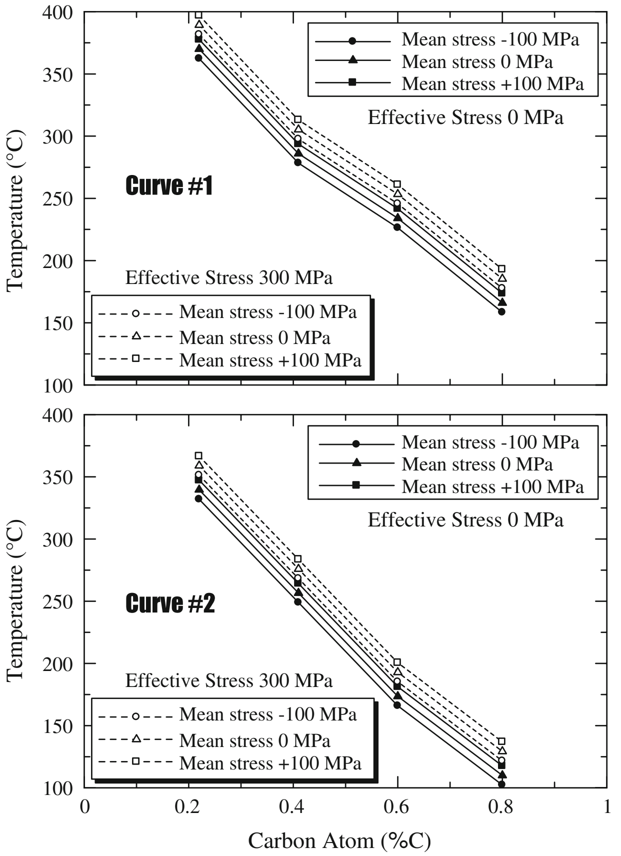

Fig. 4 Kinetics transformation during quenching as function of stress, carbon content, and temperature from 0% (*curve #1*) to 50% (*curve #2*) transformed volume fraction of martensite

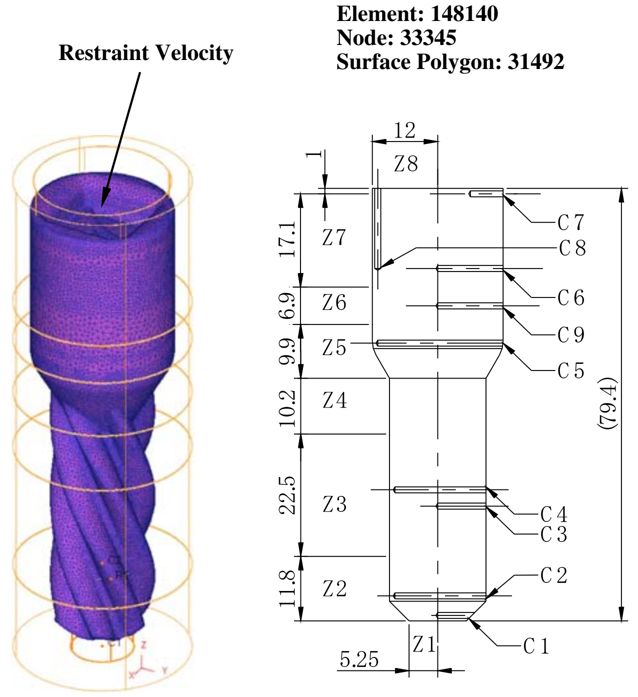

Fig. 5 Three-dimensional helical gear model with eight HTC zones as surface thermal boundary and restraint velocity boundary condition

$$\xi_B = 1 - \exp\{-kt^n\} \qquad \text{(Eq 10)}$$

Parameter for this calculation is based on TTT Data mode (Start and End curves), where ξ_B is bainite volume fraction, t is cooling time, k and n are material constant taken from start volume fraction 1% and end volume fraction 99% in which logarithm of transformation time is function of temperature, stress, and carbon content. Transformation plasticity is incorporated using Desalos model (Ref 21). The coefficient of transformation plasticity for bainite and martensite is assumed from SCr440H steel as 8.5×10^{-5} MPa^{-1} and 7.4×10^{-5} MPa^{-1}, respectively (Ref 22). It is because the coefficient of transformation plasticity of the martensite is difficult to be measured in SCr420H due to the less density of carbon content (0.21%C). It is apparent that the influence of transformation plasticity is significant to the accuracy of predicted distortion (Ref 23).

Under step-by-step time integration with constant time increment in the solution step, deformation, heat transfer, phase transformation, and diffusion were calculated during heating to 850 °C whereas, heat transfer, phase transformation, and deformation were calculated during oil quenching. Newton-Raphson iteration calculated the deformation under sparse solver, whereas calculation of temperature was done under conjugate-gradient solver. Computer resource with Pentium 4 CPU, 3.2 GHz, 2.0 GB RAM was used to simulate the 3D model. Total simulation elapsed time needed was 63 h for gas carburizing oil quenching process and 25 h for through oil quenching process.

3.3 Model and Boundary Condition

The nonaxisymmetrical three-dimensional model is built in 148140 tetrahedral finite elements, 33345 nodes, and 31492 surface polygons. To consider model accuracy, the division of the region by elements should be finer in the surface than in the core (Fig. 5). Considering complex model with fine discretion including transformation kinetics, calculation of total residual stress and strain is assumed as kinematics hardening rule condition (Ref 24). Velocity boundary condition is in restraint top position of *X*-, *Y*-, and *Z*-axis. Thermal boundary condition is zone-based heat transfer coefficient (HTC) estimated from cooling curve data of oil-quenched SUS304 gear blank. Z1-Z8 and C1-C9 denote HTC from zone 1 to zone 8 and thermocouple position from Nos. 1 to 9, respectively (Ref 23). Both thermal and velocity boundary conditions can be seen in Fig. 5. Zone-based HTC employed on the model can be seen in Fig. 6 along with the uniform HTC estimated from silver probe. This uniform HTC was used for basis calculation of zone-based HTC by using iterative modification method (Ref 25).

3.4 Stress-Strain Relationship

The expression for calculating plastic flow stress as a function of individual phase of austenitic, bainitic, and martensitic structure is given in Eq 11.

$$\bar{\sigma} = Y(T, C) + H(T, C)\bar{\varepsilon} \qquad \text{(Eq 11)}$$

Here, $\bar{\sigma}$ = flow stress, Y = yield strength, H = hardening modulus, both are function of T (temperature) and C (carbon content), and $\bar{\varepsilon}$ = effective plastic strain.

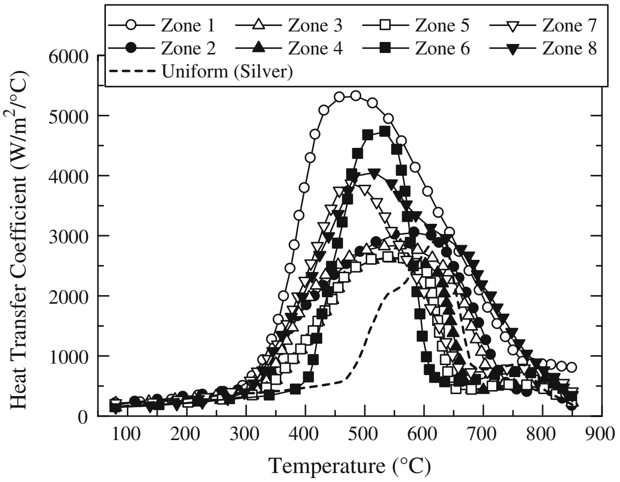

Fig. 6 Uniform HTC estimated from silver probe and modified HTC estimated from SUS304 gear blank

Total strain rate corresponding to the actual distortion directly is assumed to be divided into thermal, elastic, plastic, phase transformation, transformation plasticity, and creep strain rates according to Eq 12. This expression assumes phase transformation kinetics on elasto-plastic problems considering the infinitesimally small displacement and strain.

$$\dot{\varepsilon}_{ij} = \dot{\varepsilon}^{t}_{ij} + \dot{\varepsilon}^{e}_{ij} + \dot{\varepsilon}^{p}_{ij} + \dot{\varepsilon}^{tr}_{ij} + \dot{\varepsilon}^{tp}_{ij} + \dot{\varepsilon}^{c}_{ij} \qquad \text{(Eq 12)}$$

Time differentiation of thermal strain is related to the instantaneous thermal expansion coefficient α and the temperature change $\Delta\dot{T}$.

$$\dot{\varepsilon}^{t}_{ij} = \alpha\Delta\dot{T}\delta_{ij} \qquad \text{(Eq 13)}$$

The coefficient of thermal expansion is expressed as the function of carbon content and volume fraction of the microstructure I-th.

$$\alpha = \sum_{I=1}^{N}\left[\frac{\xi_I}{C_2 - C_1}\{(C_2 - C)\alpha_{I1} + (C - C_1)\alpha_{I2}\}\right] \qquad \text{(Eq 14)}$$

The elastic strain rate is normally expressed as:

$$\dot{\varepsilon}^{e}_{ij} = \frac{1+v}{E}\dot{\sigma}_{ij} - \frac{v}{E}\dot{\sigma}_{kk}\delta_{ij} \qquad \text{(Eq 15)}$$

Here, E and v are Young's modulus and Poisson's ratio, respectively. In the carburizing-quenching simulation, $(1+\upsilon)/E$, υ/E, and α are expressed as function of carbon content and volume fraction of microstructure as:

$$\frac{1+v}{E} = \sum_{I=1}^{N}\left[\frac{\xi_I}{C_2 - C_1}\left\{(C_2 - C)\frac{1+\upsilon_{I1}}{E_{I1}} + (C - C_1)\frac{1+\upsilon_{I2}}{E_{I2}}\right\}\right] \qquad \text{(Eq 16)}$$

$$\frac{v}{E} = \sum_{I=1}^{N}\left[\frac{\xi_I}{C_2 - C_1}\left\{(C_2 - C)\frac{1+\upsilon_{I1}}{E_{I1}} + (C - C_1)\frac{1+\upsilon_{I2}}{E_{I2}}\right\}\right] \qquad \text{(Eq 17)}$$

The plastic strain rate is reduced to the form when employing temperature-dependent materials parameters.

$$\dot{\varepsilon}^{p}_{ij} = \hat{G}\left(\frac{\partial F}{\partial \sigma_{kl}}\dot{\sigma}_{kl} + \frac{\partial F}{\partial T}\dot{T} + \sum\frac{\partial F}{\partial \xi_{IJ}}\dot{\xi}_{IJ} + \frac{\partial F}{\partial C}\dot{C}\right)\frac{\partial F}{\partial \sigma_{ij}} \qquad \text{(Eq 18)}$$

$$\frac{1}{\hat{G}} = -\left[\frac{\partial F}{\partial \varepsilon^{p}_{mn}} + \frac{\partial F}{\partial \kappa}\sigma_{mn}\right]\frac{\partial F}{\partial \sigma_{mn}} \qquad \text{(Eq 19)}$$

Here, F is the temperature-dependent yield function.

$$F \equiv f(T, C, \sigma_{ij}, \varepsilon^{P}, \xi_I, \kappa) \qquad \text{(Eq 20)}$$

Here, κ is the hardening parameter.

Strain rate due to microstructural dilatation is given by:

$$\dot{\varepsilon}^{tr}_{ij} = \sum_{I=1}^{N}\beta_{IJ}\dot{\xi}_{IJ}\delta_{ij} \qquad \text{(Eq 21)}$$

Here, β_{IJ} is the coefficient of phase transformation in fractional length change due to phase change from I to J instantaneously. $\dot{\xi}_{IJ}$ is the volume fraction rate of phase transformation which is time differentiation of the transformation volume fraction from phase I to J.

Transformation plasticity is the phenomenon of accelerated plastic deformation caused by a low level of applied stress during phase transformation. In addition to the coupling effects between stress and phase transformation, this phenomenon is also expected to significantly influence the stress-strain distribution during quenching. Stated by Desalos et al., the transformation plasticity strain rate $\dot{\varepsilon}^{tp}_{ij}$ is determined as follows (Ref 21):

$$\dot{\varepsilon}^{tp}_{ij} = \frac{3}{2}\sum_{I=1}^{N}K_{IJ}h(\xi_{IJ})\dot{\xi}_{IJ}S_{ij}, \quad h(\xi_{IJ}) = 2(1 - \xi_{IJ}) \qquad \text{(Eq 22)}$$

Here, K_{IJ} is the coefficient of transformation plasticity for diffusionless martensitic or diffusion bainitic transformation which may be identified by experimental results depended upon the dilatation-temperature diagrams. $h(\xi_{IJ})$ is the contribution from transformation progress to the transformation plasticity strain. $\dot{\xi}_{IJ}$ is the phase transformation rate and S_{ij} is the shear stress.

The creep strain rate is not assumed because there is no significant external loading during both heat treating processes, except the weight of helical gear itself that is neglected.

4. Results and Discussion

4.1 Distortion and Displacement Distribution

Figure 7 shows the reference point for measuring distortion (A-B is 22 mm long and total length is 80.6 mm long) and half model for tracking point. Reference point A and B are located at 42 and 64 mm from top of the helical gear which corresponds to nodal tracking at node 21393 and node 11758, respectively. Total length is measured from top and bottom of the gear which corresponds to nodal tracking at the highest node 31084 and the lowest node 651. Among 20 representative tracking points as shown in RH side of Fig. 7, there are seven important tracking points represented by surface (P1, P20), subsurface (P2, P19), and inner side (P7, P11, P15) to observe time-dependent displacement, temperature, martensite, retained austenite, stress, and strain. P1 (0 mm) and P20 (80.6 mm) are

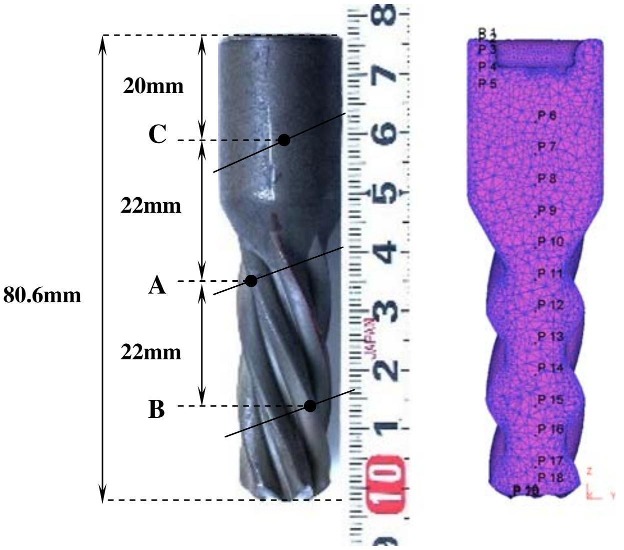

Fig. 7 Measured location of A-B distance and total length (*LH side*) and 20 tracking points on half model (*RH side*) for predicted results

located at surface. P2 (1 mm) and P19 (79.6 mm) are 1 mm subsurface to represent the case depth of carburized layer. P7, P11, and P15 are located at 20 mm (C), 42 mm (A), and 64 mm (B) from top of the gear, respectively.

Measured axial distortion (change of length) at A-B distance and total length as well as the predicted one by three simulations are shown in Fig. 8. Simulations #1, #2, and #3 are represented by the results of prediction by case harden, prediction by case harden-NoTP, and prediction by through harden, respectively. By observing the predicted value that is still within the range of measured value, simulations #1, #2, and #3 give good agreement in predicting the distortion of A-B distance. However, only simulation #1 gives good agreement in predicting the distortion of total length.

The measured axial distortion (change of length) at A-B distance and total length as well as the predicted axial distortions by three simulation types are shown in Fig. 8. Notation of #0, #1, #2, and #3 represents the measured results, the predicted results by simulations #1, #2, and #3, respectively. A-B distance and total length were marked and measured before and after conducting the case-hardening process. There were five specimens measured by using a LEITZ PMM866 Coordinate Measuring Machine. Measured distortion on A-B distance is within negative and positive value (−0.0184 and +0.3591 mm) having mean positive value (+0.1673 mm), whereas total length is within both negative value (−0.4227 and −0.0271 mm) having mean negative value (−0.1793 mm).

The predicted distortion on A-B distance is −0.0253 mm by simulation #1, +0.0454 mm by simulation #2, and +0.0072 mm by simulation #3, respectively, indicating that all simulation results have good agreement with the measured results. Namely, the predicted results are within the range of measured results. The predicted distortion on total length is −0.0404 mm by simulation #1, +0.1762 mm by simulation #2, and +0.0877 mm by simulation #3, respectively, indicating that simulation #1 have acceptable agreement with the measured one; however, both simulations #2 and #3 give unacceptable agreement with the measured one. Namely, the predicted results by simulation #1 are within the range of measured results; however, both simulations #2 and #3 are beyond the range of measured results. By observing distortion on both A-B distance and total length, it is shown that simulation #1 gives acceptable agreement, whereas simulation #2 and #3 give unacceptable agreement. In other words, both model predictions by simulations #2 and #3 for total length exhibit opposite sign (positive value) compared to model prediction by simulation #1 (negative value). The causal factor of this phenomenon will be explained by showing the different pattern of time-dependent distribution of temperature, phase transformation, stress, and individual-total strain in the following section.

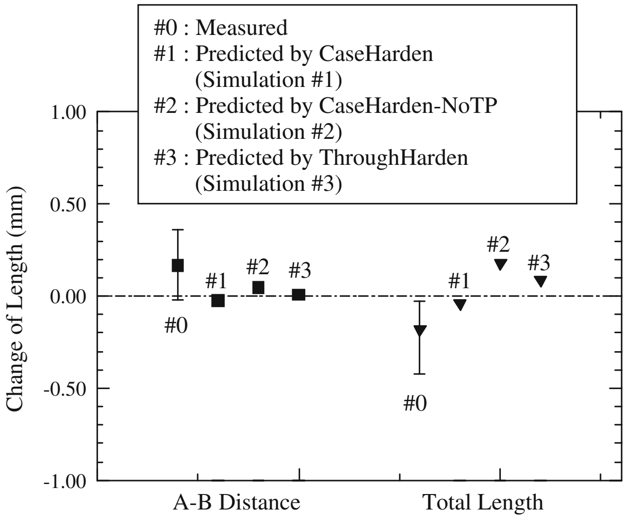

Fig. 8 Distribution of distortion of A-B distance and total length measured and predicted by three simulations

In the end of cooling after case-hardening process, the helical gear encountered axial contraction (negative value). It is apparent that the influence of transformation plasticity and the hardenability of carbon-rich layer indicated by the greater martensite in the case depth is the important factor to affect the distribution of axial distortion. Ju et al. also presented that smaller axial distortion will be resulted from calculating by with incorporation of transformation plasticity than without incorporation of transformation plasticity (Ref 26). In addition, the causal factor of tendency of axial contraction may be affected also by radial expansion of shank, dedendum, and addendum circle at observed area of 20, 42, and 64 mm cut length at the end of cooling (Ref 1).

Figure 9 shows that time-dependent axial displacement during cooling results from three simulations represented by seven important tracking points from surface of the bottom to surface of the top. Detail of seven important tracking points can be referred to Fig. 7. Because of too many lines tracked from 0.0 to 80.6 mm location, it is easy to differentiate among three simulations by summing the tracking point of P1 and P20. It can be seen from the graph that simulation #1 results in negative displacement, whereas simulations #2 and #3 result in positive displacement.

Since the heating temperature is similar at 850 °C, at the time of start cooling, simulations #1 and #2 give the same negative displacement (−0.7148 mm), whereas simulation #3 gives −0.7227 mm at P20 tracking point. It is because the axial expansion goes downward prior to cooling. As the temperature lowers by cooling, the displaced P20 goes upward till it reaches the martensite start temperature. As austenite (FCC structure) begins to transform to martensite (BCT structure) resulting in expansion in the crystal lattice, the displaced P20 goes opposite direction becoming downward at 16 s cooling time till the martensite grows maximum when the cooling time reaches 44 s. At 16 s cooling time, three simulations produce −0.0075, −0.0851, and −0.1430 mm, respectively, whereas at 44 s cooling time, three simulations produce −0.0908, −0.2247, and −0.2564 mm, respectively. As the cooling continues to final condition (end cooling), linear thermal expansion will be decreased causing displaced P20 in upward direction. In this state, three simulations give +0.0165, −0.1575, and −0.0780 mm, respectively. The influence of transformation plasticity on suppressing the displacement can be observed by comparing between simulations #1 and #2 (Fig. 9a and b). It is shown that incorporation of the transformation plasticity will result in more negative displacement. Besserdich et al. and Inoue et al. have shown that the more compressive residual stress is employed, the more negative axial strain will be produced during phase transformation (Ref 27, 28). Simulations #1 and #3 (Fig. 9a and c) are compared to show the influence of case-hardening process over through-hardening process in suppressing the displacement. Axial compressive residual stress is introduced by increasing the volume fraction of martensite due to carbon-rich layer during carburizing process. It is, therefore, the more compressive residual stress is produced, the more negative axial displacement will occur (Ref 27).

4.2 Time-Dependent Temperature and Phase Transformation

The surface and subsurface of bottom region are cooled faster than top region because of different surface heat transfer and heat conduction related to lumped-mass effect, as shown in Fig. 6. Distribution of time-dependent temperature or temperature change during cooling from 3 to 163 s can be seen in Fig. 10. It is also clearly shown that the temperature drop in toothed area (−42 and −64 mm) progresses faster than that in shank area (−20 mm).

Among the results of temperature prediction from three simulations, there is no significant different type of temperature change during cooling. It is because the calculation of thermal history, though coupled with phase transformation producing

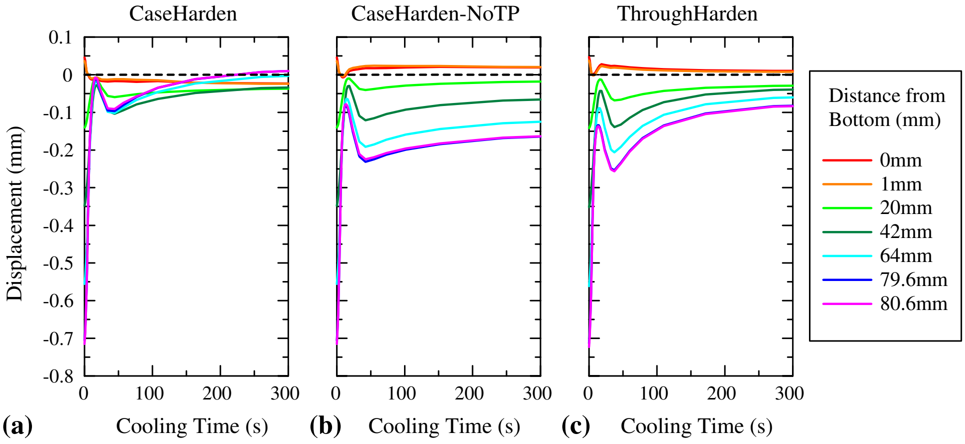

Fig. 9 Distribution of time-dependent displacement predicted by three simulations

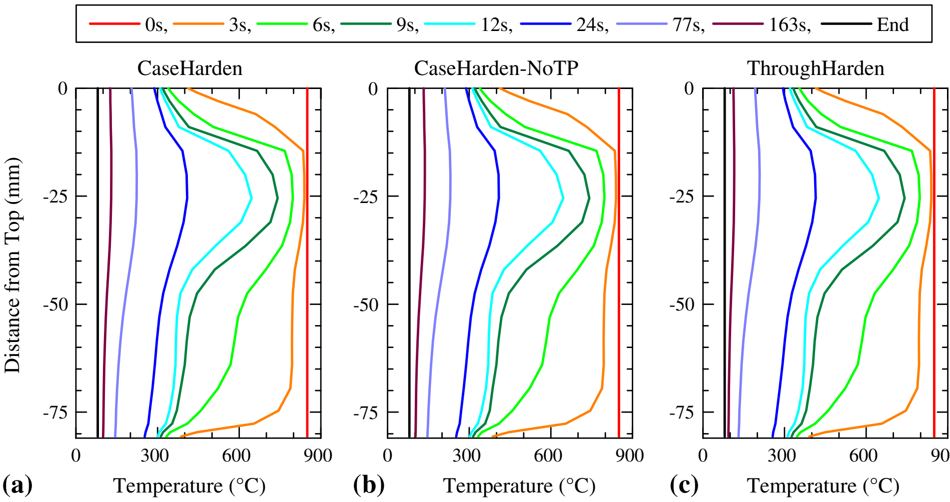

Fig. 10 Distribution of time-dependent temperature predicted by three simulations

different volume fraction of martensite in case hardening (simulations #1 and #2) and through hardening (simulation #3), is mainly affected by similar zone-based HTC employed. However, between case hardening and through hardening show the significant difference of martensite and retained austenite volume fraction (Fig. 11 and 12).

Figures 11 and 12 show the formation of martensite and retained austenite as function of cooling time from bottom to top region by three simulations, respectively. There is no significant difference of volume fraction of martensite and retained austenite formed as shown by Fig. 11(a, b) and 12(a, b) whereas, between Fig. 11(a-c) and 12(a-c) differ significantly as the process is different (case hardening and through hardening). At 1 mm subsurface where the case depth lies, the martensite and retained austenite are greater at case-hardened section than at through-hardened section. Beyond the case depth layer, the distribution of martensite becomes lower and no significant difference of volume fraction has been observed among the results from three simulations (Fig. 11). Retained austenite does not appear at the area beyond the case depth layer and all sections of through-hardened gear do not show any retained austenite (Fig. 12).

As shown in Fig. 11(a) and (b), during 9 s cooling time observed at P20 tracking point, martensite is transformed at subsurface firstly then followed by at surface indicating that, there is a time-lag of martensite formation from subsurface (15.6% and 22.6%) to surface (0%), respectively. Martensite starts at subsurface earlier because of austenite retention at carbon-rich layer (64.9% and 58.5% at subsurface and 100% at surface), respectively, as shown by Fig. 12(a) and (b). However, martensite starts from the surface then to the core as usual during through-hardening process (Fig. 11c). The different pattern of final distribution of martensite volume fraction correlates with the content of retained austenite in the case depth. Without further sub-zero treatment, oil quenching process produces a significant amount of retained austenite (Ref 29, 30). A significant amount of austenite is retained in the surface because of the increased carbon content (Ref 31, 32). Chemical stabilization due to the

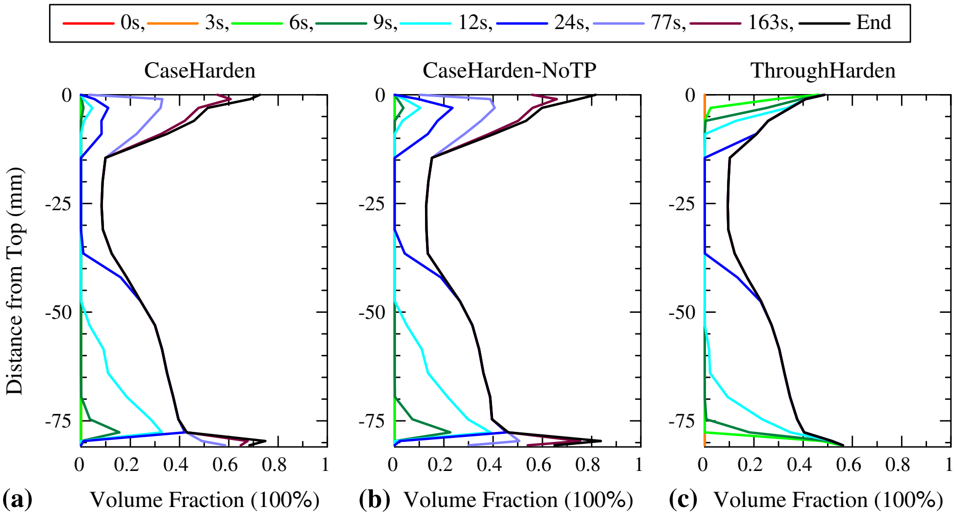

Fig. 11 Distribution of time-dependent formation of martensite predicted by three simulations

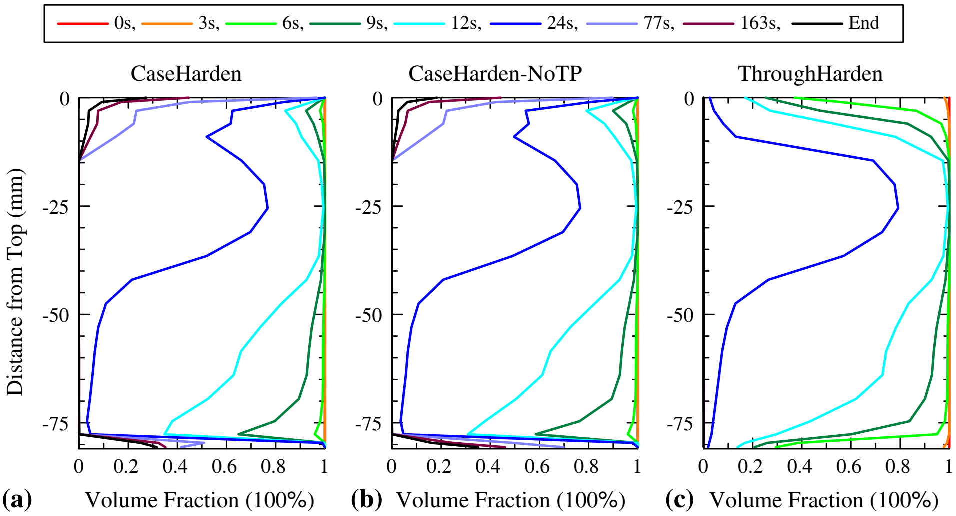

Fig. 12 Distribution of time-dependent formation of retained austenite predicted by three simulations

enrichment of carbon in the retained austenite is the most important mechanism (Ref 33). At the end of cooling time in P20 tracking point, predicted retained austenite is about 32% resulting from simulations #1 and #2, whereas 0% retained austenite is predicted by simulation #3. No retained austenite is predicted at over 1 mm case depth. Hence, by coupling with the effect of transformation plasticity, it is shown that martensite layer in the case depth may act as a contributing factor to the different amount of displacement (Fig. 9).

4.3 Time-Dependent Stress

Figure 13(a-c) shows predicted time-dependent axial stress generated during oil quenching using simulations #1, #2, and #3, respectively. Generated axial stress varies according to the effect of transformation plasticity and the amount of martensite volume fraction in the case depth layer. The residual stresses at the end of cooling are in accordance with their inherent characteristics due to lower Ms temperature at surface and subsurface in case-hardened gear and higher Ms temperature in through-hardened gear.

The influence of transformation plasticity can be seen by comparing Fig. 13(a) and (b) at P19 tracking point. Before 12 s cooling time, it seems that the stress change is almost similar pattern because the amount of maximum transformed martensite is 32.8% and 38.9% in Fig. 11(a) and (b), respectively. In this amount of transformed martensite, the transformation-induced plasticity is small enough to affect the pattern of stress change. After 24 s to the end of cooling time, when the martensite grows to reach 74.8% and 83.7% maximum volume fraction shown in Fig. 11(a) and (b), respectively, the effect of transformation plasticity significantly affects the pattern of stress change. Since the equilibrium condition of axial residual stress prevails on surface and subsurface in *z*-axis, P1, P2, P19, and P20 tracking points have negligible amount of residual stress. Therefore, only P7, P11, and P15 tracking point of axial residual stress will be considered. At the end of cooling time, it can be seen that transformation plasticity has influence in suppressing the residual stress generated as much as −7, +228, and +227 MPa (simulation #1) and +348, +369, and +476 MPa (simulation #2), respectively.

By taking transformation plasticity into account during both simulations #1 and #3, the effect of martensite volume fraction in the case depth layer on the pattern of stress distribution can be seen by comparing Fig. 13(a) and (c). Since the carbon-rich layer lowers the Ms temperature in the case-hardened gear, austenite transforms to martensite faster at subsurface than at surface causing tension at the surface-subsurface and compression at the core during 9 s cooling time (Fig. 11a). After that, martensite grows at surface-subsurface causing compression at the surface and tension at the core (Ref 34). The amount of martensite at the case depth has significant impact on the different distribution of stress started from 9 s cooling time. At the end of cooling time, compared to the results of simulation #1, the smaller residual stress has been observed on the results of simulation #3, i.e., the residual stress generated is −151, −15, and −17 MPa at P7, P11, and P15 tracking points, respectively.

4.4 Time-Dependent Axial Strain

The negative axial displacement on the case-hardened gear in this study will be sufficiently analyzed by observing time-dependent axial strain. Figure 14 shows time-dependent axial strain resulting from three simulations. To simplify the notification on Fig. 14, each simulations #1, #2, and #3 has its thermal, elastic, plastic, phase transformation, transformation plasticity, and total strain noted as (a), (b), (c), (d), (e), and (f) for simulation #1, (g), (h), (i), (j), (k), and (l) for simulation #2, and (m), (n), (o), (p), (q), and (r) for simulation #3, respectively. Although the difference of thermal strain and phase transformation strain has been clearly shown by Kang-Im, different results of both predicted strains have not been presented yet (Ref 35). Therefore, different pattern of both strains is shown in Fig. 14(a, g, m) for thermal strain and Fig. 14(d, j, p) for phase transformation strain, respectively. Phase trf and trf plasticity denote phase transformation strain and transformation plasticity strain, respectively. Because of too small strain generated during oil quenching, only elastic and plastic strain is presented in smaller scale ±0.002 mm/mm for the reason of clarity of the pattern. Others are in larger scale ±0.01 mm/mm.

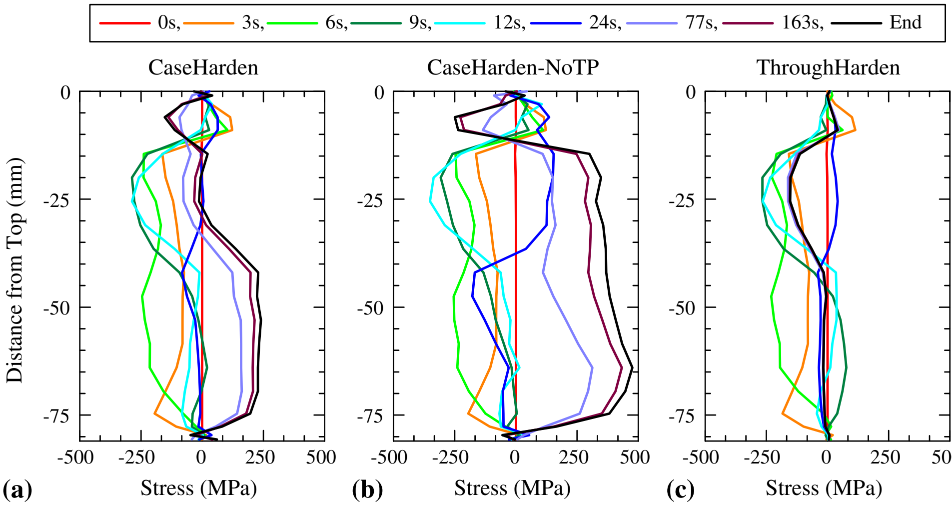

Fig. 13 Distribution of time-dependent generation of stress predicted by three simulations

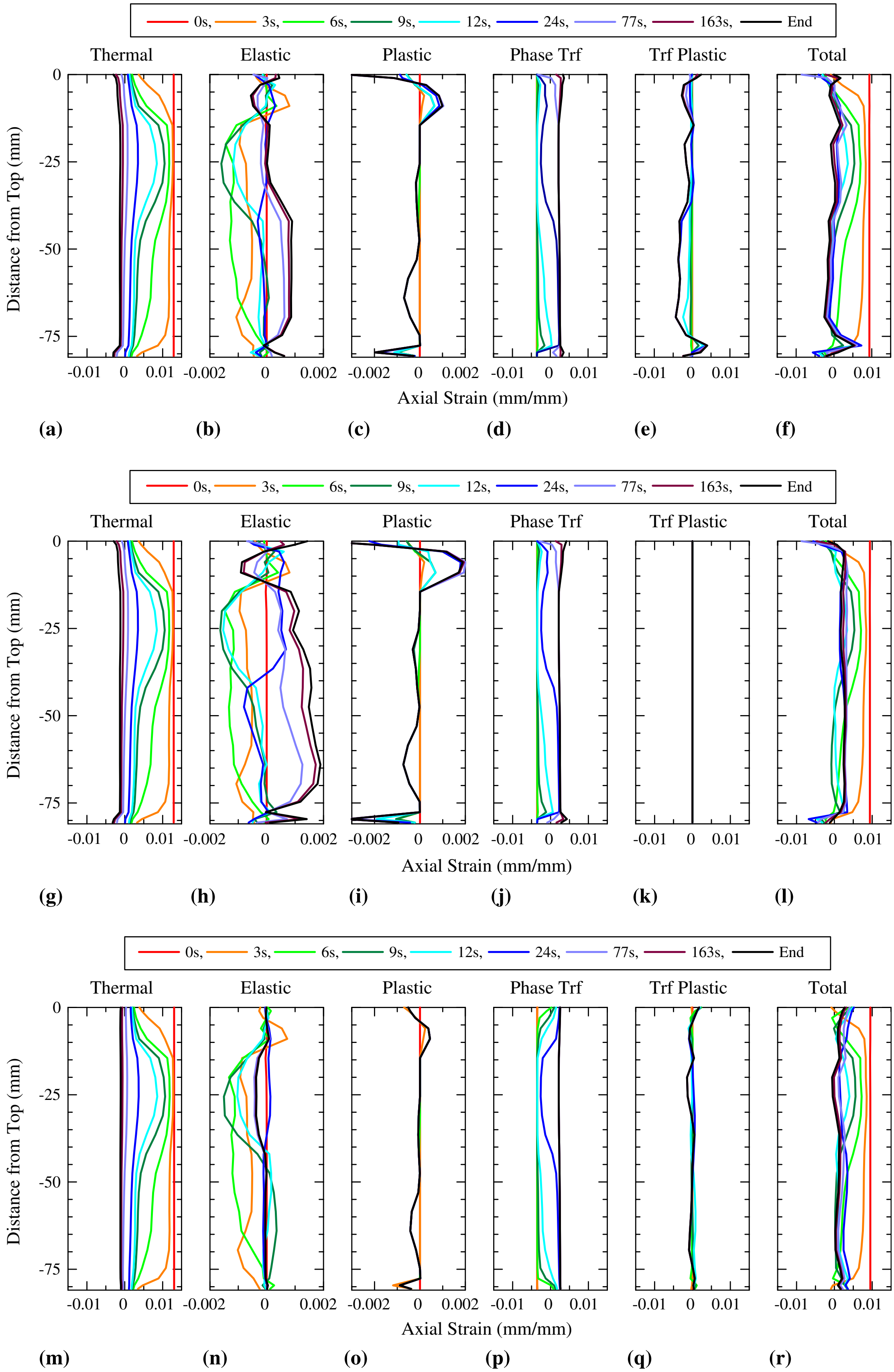

Fig. 14 Distribution of time-dependent generation of axial strain predicted by three simulations; case-hardened with TP (a-f), case-hardened without TP (g-l), through-hardened with TP (m-r). *Note*: Phase Trf and Trf plasticity are phase transformation and transformation plasticity, respectively

Figure 14(a, g, m) shows time-dependent axial thermal strain and they have completely similar pattern from 0 to 24 s cooling time because thermal strain are isotropic value. All simulations produce axial thermal strain +0.0129 at the start of cooling. There are no significant differences from 0 s to the end of cooling between simulations #1 and #2. However, by observing P1 and P20 tracking points from 77 s to the end of cooling, there are slightly bent inward (decrease strain) at both results of simulations #1 and #2, compared with almost flat at the results of simulation #3. At P20 tracking point, the final axial thermal strain indicates −0.0031 (simulations #1 and #2) and −0.0010 (simulation #3). The different thermal strain produced by case hardening and through-hardening process may be caused by the couple effect among volume fraction of martensite-retained austenite and carbon content in affecting the amount of latent heat. Zwaag et al. has shown the effect of retained austenite on decreasing strain (Ref 36).

Since residual stress corresponds to elastic strain by linear relationship of Eq 15, mechanism of stress generation will be studied by analyzing the time-dependent elastic strain. Therefore, the origin of stress pattern may be correlated with the elastic strain changes. Distribution of elastic strain varies during cooling as shown in Fig. 14(b, h, n). The final patterns of strain distribution show almost similar with the final patterns of residual stress distribution. Axial elastic strain observed at P7, P11, and P15 tracking points corresponds to the axial residual stress distribution as shown in Fig. 13. Since the equilibrium state of axial stress at the surface and subsurface facing axial direction, P1, P2, P19, and P20 tracking points also inform the negligible amount of axial elastic strain. Like distribution of residual stress pattern, transformation plasticity affects the suppression of elastic strain, and the higher martensite at case depth affects the greater difference of elastic strain between surface and inner area.

Plastic strain will be generated when the stress condition has surpassed the yield strength of the body. It seems that the plastic strain generation at P7 and P11 tracking points is almost negligible during cooling, except the area where there is more severe cooling. P15 tracking point cools faster according to the higher HTC (Fig. 6). In addition to the faster cooling caused by lumped-mass effect, volume fraction of martensite and retained austenite increase the plastic strain at P1, P2, P19, and P20 tracking points as shown in Fig. 14(c, o). The effect of martensite and retained austenite formed on the case depth can be clearly shown by comparing the results of simulations #1 and #3. Transformation plasticity has an effect in reducing the amount plastic strain as shown in Fig. 14(c, i). The influence of transformation plasticity in suppressing the plastic strain in the case depth may be correlated with the incorporation of shear stress induced during phase transformation (Eq 22). Transformation plasticity can be induced by both stress and plastic strain. Stress-affected transformation can explain much of the variation in retained austenite as a function of plastic strain (Ref 37).

Figure 14(d, j, p) shows time-dependent axial phase transformation strains. On condition that volume fraction is similar within the body, these strains are also completely similar pattern from 0 to 6 s cooling time because phase transformation strain is isotropic value. All simulations produce axial phase transformation strain −0.0035 at 0 s cooling time. There are no significant differences from 0 s to end cooling time between simulations #1 and #2. However, by observing at P1 and P20 tracking points at 9 s cooling time, there is time-lag of phase transformation strain at both results of simulations #1 and #2. It is because of lower Ms temperature in case depth, compared with the results of simulation #3. It is well known that the greater volume fraction of martensite, the more dilatation as results of more elongated BCT structure of martensite (Ref 18). Therefore, in the end of cooling at P1 and P20 tracking points, simulations #1 and #2 produce more positive strain (+0.0031 and +0.0033) than that of the results of simulation #3 (+0.0026 and +0.0025), respectively.

The phenomenon of transformation plasticity has attracted many authors since the comprehensive study conducted by Greenwood-Johnson (Ref 38). Transformation plasticity has great effect to the generation of total strain affecting the final displacement. At the end of cooling, the pattern of axial total strain has almost similar to axial transformation plasticity strain as shown in Fig. 14(e, f, q, r). To study the effect of transformation plasticity on the total strain distribution, this phenomenon is deliberately omitted in the simulation #2. Therefore, Fig. 14(k) has nil transformation plasticity strain. From 0 to 24 s of cooling time, the transformation plasticity strain has instantaneous change according to cooling time and it reaches the final pattern with almost no change at 77 s of cooling time. At this time, the maximum temperature (223 °C) is lower than Ms temperature (417 °C) in all sections of the gear. The influence of transformed volume fraction of martensite in increasing the transformation plasticity strain can be seen by comparing Fig. 14(e) and (q). At the end of cooling, it is apparent that case-hardening process produces greater axial transformation plasticity strain than through-hardening process. This analysis is supported by the experiment conducted by Ju et al. in determining the parameter of transformation plasticity due to the generation of martensite volume fraction (Ref 39).

Relating to the negative displacement on axial direction, the change of axial total strain is equal to the instantaneous length change on all tracked points from surface, subsurface, and inner part of the helical gear. The integration of axial total strain among them results in displacement of the total length. Origin of the length changes can be analyzed by observing the predicted axial total strain changes. The strong effect of thermal strain in building the total strain is presented from 0 to 3 s cooling time. Then, according to the strain equilibrium condition in Eq 12, local changes of both thermal strain and phase transformation strain should be compensated by elastic strain initially, plastic strain when yield strength is surpassed producing plasticity, and transformation plasticity strain generated during phase transformations as function of stress. Since the axial displacement or axial distortion is proportional to the axial total strains (Ref 40), the predicted change of length, which is in good agreement shown in Fig. 8, can be analyzed by observing the axial total strain at the end of cooling. By tracking between node 31084 and node 651, total strain of simulation #1, #2, and #3 is −0.0052, +0.0338, and +0.0209, respectively, contributing to the change of total length of −0.0404, +0.1762, and +0.0877 mm, respectively. Finally, the mechanism of the change of length during cooling in the helical gear has been shown by presenting the time-dependent axial total strain depicted in Fig. 14.

The industrial implication of these results and benefits of such modeling exercise will have an impact on understanding the effect of transformation plasticity and carbon-rich induced martensite layer in distortion behavior of a case-hardened helical gear. The combination of shank and gear profile, particularly the helix angle, may affect the negative axial distortion in total length. Successful prediction in this study clearly identify that the anticipation of negative axial distortion during fabrication of such helical gear will be a beneficial factor to the optimum design. The usage of computer simulation in the design and fabrication has proven to be an excellent method for reducing trial-and-error costs and for anticipating the unwanted distortion. Therefore, the anticipation of finishing operations for a heat-treated helical gear can also be predicted. Thus, it will significantly reduce machining time and waste.

5. Conclusions

The contraction of total length (negative displacement) after case hardening has been analyzed by conducting three simulations, e.g., case-hardening process incorporating transformation plasticity (simulation #1), case-hardening process not incorporating transformation plasticity (simulation #2), and through-hardening process incorporating transformation plasticity (simulation #3). The conclusions can be summarized as follows:

- Reasonably good agreement between measured and predicted distortion (the change of length after case hardening) is presented. There is no significant difference in predicting A-B distance from the results of three simulations. However, in predicting total length, simulation #1 gives the highest accuracy, in which the results of prediction are in negative value.
- Axial contraction occurring after case-hardening process can be analyzed by predicting the axial displacement which corresponds to the time-dependent total and individual strain. By observing the integral of axial total strain at the end of cooling, axial contraction of the case-hardened helical gear can be understood. Transformation plasticity strain has strong influence to the pattern of final total strain illustrated by simulations #1 and #3.
- Compared with the results from through-hardening process, martensite combined with retained austenite in the case depth as a result from case-hardening process has shown a profound effect to the suppression of total strain.
- The major limitation of the model is that through-hardening process is conducted virtually. Further experiment on through-hardening process is necessary to be done. And also, since the complexity of gear profile with helix angle needs a representative position and exact orientation, measurement of surface and subsurface residual stress has not been performed. Due to lack of this experimental evidence, measurement of residual stress is required to validate the model.

Acknowledgments

The authors would like to express their gratitude to Scientific Forming Technologies Co. (USA) and Yamanaka Engineering Co. Ltd. (Japan) for the cooperation with the numerical simulation by FEM code of DEFORM-HT. This research was partially supported by MEXT: Ministry of Education, Culture, Sports, Science, and Technology, Grant-in-Aid for Scientific Research (C), 2006, No. 18560688.

References

1. A. Sugianto, M. Narazaki, M. Kogawara, S.Y. Kim, and S. Kubota, Distortion Mechanism During Carburising-Quenching of SCr420H Helical Gear, *Proc. 16th IFHTSE Congress*, Oct 30-Nov 1, 2007 (Brisbane), Materials Australia, 2007, IFHTSE07-257
2. S.Y. Kim, S. Kubota, and M. Yamanaka, Application of CAE in Cold Forging and Heat Treatment Processes for Manufacturing of Precision Helical Gear Part, *J. Mater. Process. Technol.*, 2008, **201**(1–3), p 25–31
3. H. Fujio, M. Takahashi, and H. Yushio, Influence of Hardenability on Helical Gear Distortions Caused by Hardening, *Nippon Kikai Gakkai Ronbunshu, C Hen*, 1986, **52**(480), p 2181–2186 (in Japanese)
4. J. Fluhrer, *DEFORM-HT 2D & 3D Users Manual*, Scientific Forming Technologies Co, Columbus, OH, 2008
5. K. Arimoto, T. Horino, F. Ikuta, C. Jin, S. Tamura, and M. Narazaki, Explanation of the Origin of Distortion and Residual Stress in Water Quenched Cylinders Using Computer Simulation, *J. ASTM Int.*, 2006, **3**(5), JAI14204
6. Y. Watanabe, D.Y. Ju, H. Shichino, K. Okamura, M. Narazaki, H. Kanamori, K. Ichitani, and T. Inoue, Cooperative Research to Optimize Heat Treating Process Condition by Computer-Based Technology, *Solid State Phenom.*, 2006, **118**, p 349–354
7. K. Arimoto and S. Yamanaka, Explanation of the Origin of Distortion and Residual Stress in Carburized Ring Using Computer Simulation, *Proc. 15th IFHTSE Congress*, Sep 25-29, 2006 (Vienna), ASMET, 2006, MN-7
8. C. Mgbokwere and M. Callabresi, Numerical Simulation of a Heat Treated Ring Gear Blank, *J. Eng. Mater. Technol.*, 2000, **122**(3), p 305–314
9. D.Y. Ju, Y. Ito, and T. Inoue, Simulation and Verification of Residual Stress and Distortion in Carburizing-Quenching Process of a Gear Shaft, *Proc. 4th Int. Conf. on Quenching and Control of Distortion*, May 20-23, 2003 (Beijing), ASM International, 2003, p 291–296
10. R. Mukai and D.Y. Ju, Simulation of Carburizing-Quenching of a Gear, Effect of Carbon Content on Residual Stress and Distortion, *J. Phys. IV Fr.*, 2004, **120**, p 489–497
11. J.R. Cho, W.J. Kang, M.G. Kim, J.H. Lee, Y.S. Lee, and W.B. Bae, Distortions Induced by Heat Treatment of Automotive Bevel Gears, *J. Mater. Process. Technol.*, 2004, **153–154**(1–3), p 476–481
12. T. Sugimoto and Y. Watanabe, Evaluation of Important Factors Affecting Quench Distortion of Carburized Hypoid Gear with Shaft by Using Computer Simulation Method, *Trans. Mater. Heat Treat.*, 2004, **25**(5), p 480–485
13. A.K. Rakhit, *Heat Treatment of Gears*, ASM International, Materials Park, OH, 2000, p 91–100
14. A. Sugianto, M. Narazaki, M. Kogawara, S.Y. Kim, and S. Kubota, Numerical Simulation and Experimental Verification of Carburizing-Quenching Process of SCr420H Steel Helical Gear, *J. Mater. Process. Technol.*, 2009, **209**(7), p 3597–3609
15. R.M. Bowen, Theory of Mixtures, in *Continuum Physics*, Vol. 3, A.C. Eringen, Ed., Academic Press, 1976, p 2–129
16. T. Inoue, D.Y. Ju, and K. Arimoto, Metallo-Thermo-Mechanical Simulation of Quenching Process, Theory and Implementation of Computer Code HEARTS, *Proc. 1st Int. Conf. on Quenching and Control of Distortion*, Sep 22–25, 1992 (Chicago), ASM International, 1992, p 205–212
17. C.S. Roberts, Effects of Carbon on the Volume Fractions and Lattice Parameters of Retained Austenite and Martensite, *Trans. AIME*, 1953, **197**, p 203–204
18. W.D. Callister Jr., *Materials Science and Engineering: An Introduction*, Wiley, New York, 2000, p 98–100
19. C.L. Magee, *The Nucleation of Martensite in Phase Transformations*, ASM International, Metals Park, OH, 1970, p 115–156
20. W.A. Johnson and R.F. Mehl, Reaction Kinetics in Processes of Nucleation and Growth, *Trans. AIME*, 1939, **135**, p 416–458
21. Y. Desalos, J. Giusti, and F. Gunsberg, "Deformations et contraintes lors du traitement thermique de pieces en acier," Report 902, IRSID, St-Germain-en-Laye, 1982 (in French)
22. M. Narazaki, T. Okamura, and H. Sichino, "Validation of Material Property Data by Comparison Between Simulation and Experimental Results of Jominy End Quenching," Report B-1, JSHT & JSMS, Kyoto, 2004

23. A. Sugianto, M. Narazaki, M. Kogawara, S.Y. Kim, and S. Kubota, The Effect of Transformation Plasticity on Prediction of Tooth Distortion of Heat-Treated Helical Gear, *Mater. Sci. Forum*, 2007, **561–565**(Part 3), p 1853–1856
24. Fletcher A.J., *Thermal Stress and Strain Generation in Heat Treatment*, Elsevier Sciences, New York, 1989, p 118–138
25. D.Y. Ju and M. Narazaki, Simulation and Experimental Verification of Residual Stress and Distortion During Quenching of Steel, *Proc. 20th ASM Heat Treating Society Conf.*, Oct 9–12, 2000 (St. Louis), ASM International, 2000, p 441–447
26. D.Y. Ju, W.M. Zhang, and Y. Zhang, Modeling and Experimental Verification of Martensitic Transformation Plastic Behavior in Carbon Steel for Quenching Process, *Mater. Sci. Eng. A*, 2006, **438–440**, p 246–250 (Special issue)
27. G. Besserdich, B. Scholtes, H. Muller, and E. Macherauch, Consequence of Transformation Plasticity on the Development of Residual Stress and Distortion During Martensitic Hardening of ASE 4140 Steel Cylinder, *Steel Res. Int.*, 1994, **65**(1), p 41–46
28. T. Inoue, Z.G. Wang, and K. Miyao, Thermal and Phase Transformation Stresses in a Carburized-Quenched Gear Wheel, *Proc. 32nd Japan Congress on Material Research* (Kyoto), JSMS, 1989, p 21–26
29. B.L. Ferguson, Z. Li, and A.M. Freborg, Modeling Heat Treatment of Steel Parts, *Comput. Mater. Sci.*, 2005, **34**(3), p 274–281
30. A.K. Rakhit, *Heat Treatment of Gears*, ASM International, Materials Park, OH, 2000, p 68–76
31. N. Luzginova, L. Zhao, and J. Sietsma, Evolution and Thermal Stability of Retained Austenite in SAE 52100 Bainitic Steel, *Mater. Sci. Eng. A*, 2007, **448**(1–2), p 104–110
32. D. Rojko and V. Gliha, Simulations of Transformation Kinetics in a Multi-Pass Weld, *Mater. Manuf. Process.*, 2005, **20**(5), p 833–849
33. J. Wang and S. Van der Zwaag, Stabilization Mechanisms of Retained Austenite in Transformation-Induced Plasticity Steel, *Metall. Mater. Trans. A*, 2001, **32**(6), p 1527–1539
34. E. Macherauch and O. Vohringer, Residual Stress After Quenching, in *Theory and Technology of Quenching*, B. Liscic, H.M. Tensi, and W. Luty, Ed., Springer-Verlag, 1992, p 155–161
35. S.H. Kang and Y.T. Im, Three-Dimensional Thermo-Elastic-Plastic Finite Element Modeling of Quenching Process of Plain-Carbon Steel in Couple with Phase Transformation, *Int. J. Mech. Sci.*, 2007, **49**(4), p 423–439
36. S. Zwaag, L. Zhao, S. Kruijver, and J. Sietsma, Thermal and Mechanical Stability of Retained Austenite in Aluminum-Containing Multiphase TRIP Steels, *ISIJ Int.*, 2002, **42**(12), p 1565–1570
37. S. Chatterjee and H.K.D.H. Bhadeshia, Transformation Induced Plasticity Assisted Steels: Stress or Strain Affected Martensitic Transformation?, *Mater. Sci. Technol.*, 2007, **23**(9), p 1101–1104
38. G.W. Greenwood and R.H. Johnson, The Deformation of Metals Under Small Stresses During Phase Transformations, *Proc. R. Soc. Lond. A*, 1965, **283**, p 403–422
39. D.Y. Ju, W.M. Zhang, and Y. Zhang, Modeling and Experimental Verification of Plastic Behavior of the Martensitic Transformation Plastic Behavior in a Carbon Steel, *Solid State Phenom.*, 2006, **118**, p 369–374
40. N.E. Dowling, *Mechanical Behavior of Materials: Engineering Methods for Deformation, Fracture, and Fatigue*, 2nd ed., Prentice Hall, Englewood Cliffs, NJ, USA, 1999, p 562–570